Chemical Engineering Journal 471 (2023) 144489

Contents lists available at ScienceDirect

Chemical Engineering Journal

journal homepage: www.elsevier.com/locate/cej

Boron monosulfide as an electrocatalyst for the oxygen evolution reaction

Linghui Li [a], Satoshi Hagiwara [b], Cheng Jiang [c], Haruki Kusaka [a], Norinobu Watanabe [a], Takeshi Fujita [d], Fumiaki Kuroda [b], Akiyasu Yamamoto [e], Masashi Miyakawa [f], Takashi Taniguchi [f], Hideo Hosono [f,g], Minoru Otani [b], Takahiro Kondo [h,i,*]

[a] Graduate School of Pure and Applied Sciences, University of Tsukuba, Tsukuba 305-8573, Japan
[b] Center for Computational Sciences, University of Tsukuba, Tsukuba 305-8571, Japan
[c] Institute of Technical and Macromolecular Chemistry, RWTH Aachen University, Aachen 52074, Germany
[d] School of Engineering Science, Kochi University of Technology, Kochi 782-8502, Japan
[e] Tokyo University of Agriculture and Technology, Tokyo 1838538, Japan
[f] Research Center for Materials Nanoarchitectonics, National Institute for Materials Science, Tsukuba 305-0044, Japan
[g] MDX Research Center for Element Strategy, Tokyo Institute of Technology, Yokohama 226-8503, Japan
[h] Department of Materials Science and Tsukuba Research Center for Energy Materials Science, Institute of Pure and Applied Sciences and R&D Center for Zero CO_2 Emission with Functional Materials, University of Tsukuba, Tsukuba 305-8573, Japan
[i] Advanced Institute for Materials Research, Tohoku University, Sendai 980-8577, Japan

ARTICLE INFO

Keywords:
Boron monosulfide
Electrocatalyst
Oxygen evolution reaction
Alkaline medium
Graphene
Renewable energy device

ABSTRACT

The current energy crisis and environmental problems associated with the use of fossil fuels necessitate a transition to clean and sustainable energy carriers like hydrogen produced by electrocatalytic water splitting. Hence, the development of robust, low-cost, and high-performance oxygen evolution reaction (OER) electrocatalysts has attracted considerable attention. Herein, an OER electrocatalyst for use in alkaline media is prepared by hybridising rhombohedral boron monosulfide with graphene to provide electronic conductivity. The catalytic activity of the electrocatalyst (overpotential of 250 mV at 10 mA cm^{-2}) is higher than those of most previously reported counterparts. Our results pave the way for the design of electrocatalysts composed of abundant elements with a wide range of applications in renewable energy devices.

1. Introduction

Fuel cells, metal–air batteries, and water electrolysers have attracted increasing attention as renewable energy technologies owing to their high theoretical energy densities [1,2]. These devices comprise two subsystems, viz. the oxygen reduction reaction (ORR), or hydrogen evolution reaction (HER) on the cathode, and the oxygen evolution reaction (OER), or oxidation of a chemical fuel on the anode. A higher energy (or overpotential) is required to overcome the kinetic hindrance associated with the OER than that for the HER, because the OER involves a four-electron transfer in contrast to the two-electron transfer process of the HER [3,4].

Since the sluggish OER kinetics restrict the practical applications of these systems for energy conversion and storage, various catalysts have been designed in the past few decades for accelerating the electrode kinetics and improving their stability in diverse electrolyte environments [5,6]. Currently, RuO_2 is considered the best OER electrocatalyst because of its superior performance in both acidic and alkaline solutions, while IrO_2 has equivalent activity and higher stability at high potentials [7]. However, these materials cannot be adopted on a large scale because of their reliance on precious metals. To address this issue, catalysts based on non-precious metals, particularly transition metals, have

Abbreviations: CB, carbon black; CHE, computational hydrogen electrode; CNT, carbon nanotube; CV, cyclic voltammetry; DFT, density functional theory; EDS, energy-dispersive X-ray spectroscopy; GCE, glassy carbon electrode; GNP, graphene nanoplate; HER, hydrogen evolution reaction; LSV, linear sweep voltammetry; NF, Ni foam; OER, oxygen evolution reaction; ORR, oxygen reduction reaction; r-BS, rhombohedral boron monosulfide; RHE, reversible hydrogen electrode; RRDE, rotating ring–disc electrode; SEM, scanning electron microscopy; STEM, scanning transmission electron microscopy; TEM, transmission electron microscopy; XRD, X-ray diffraction; XPS, X-ray photoelectron spectroscopy.

* Corresponding author at: Department of Materials Science and Tsukuba Research Center for Energy Materials Science, Institute of Pure and Applied Sciences and R&D Center for Zero CO_2 Emission with Functional Materials, University of Tsukuba, Tsukuba 305-8573, Japan.
E-mail address: takahiro@ims.tsukuba.ac.jp (T. Kondo).

https://doi.org/10.1016/j.cej.2023.144489
Received 31 March 2023; Received in revised form 27 May 2023; Accepted 27 June 2023
Available online 28 June 2023

been designed [8–11]. OER catalysts containing transition metals and metal oxides have been extensively studied [12–14]. However, most of the reported materials are limited by low conductivity, low cost-efficiency, and/or environmental toxicity. Carbon-based materials such as heteroatom-doped carbon (nitrogen-, phosphorus-, and/or sulfur-doped graphene or carbon nanotubes (CNTs)) have also been reported as electrocatalysts [15–19]. These materials are advantageous as they are composed of abundant elements. Heteroatom doping is believed to increase the OER activity by redistributing the charges on the carbon atoms [20]. Zhang et al. [16] reported nitrogen and phosphorus co-doped mesoporous nanocarbons as bifunctional OER and ORR electrocatalysts. Density functional theory (DFT) calculations indicated that the edges of nitrogen- and phosphorus-coupled graphene flakes contained OER-active sites [16]. The phosphorus-doped graphite layers produced by Liu et al. [18] demonstrated higher OER activity than most previously reported OER catalysts and featured C–O–P moieties as the primary OER-active species. However, such doped carbon nanomaterials are typically prepared using complex multistep processes such as high-energy pyrolysis and hazardous chemical treatments.

Rhombohedral boron monosulfide (r-BS) has recently been identified as a new parent material for fabricating catalysts. The structure of r-BS is similar to that of two-dimensional transition-metal dichalcogenides in that it has a layered structure with sulfur terminations on each layer [21]. In this study, we developed a promising OER electrocatalyst based on a mixture of r-BS and graphene (r-BS + G), wherein the graphene nanoplates (GNP) impart electrical conductivity to the catalyst. Multi-probe spectroscopic characterisation and electrochemical measurements confirmed that the OER activity originates purely from r-BS + G. Finally, we discussed the possible active sites in r-BS. The OER activity of the developed catalyst in an alkaline medium exceeded those of most reported catalysts such as commercial RuO_2. Our results suggest that r-BS + G, composed of abundant elements, can be utilized as a catalyst for renewable energy technologies.

2. Materials and methods

2.1. Materials

Amorphous boron (>99.5%) was prepared by the decomposition of B_2H_6 (Primary Metal Chemical Japan, Kanagawa, Japan). Sulfur (99%) was purchased from Wako Pure Chemical Industries Ltd. (Osaka, Japan). GNP (average number of layers: 5–7), Nafion (5 wt% in lower aliphatic alcohols and water), NaOH (97%), and commercial RuO_2 (99.9%) were purchased from Sigma-Aldrich (Japan). Nickel foam (200 × 300 × 1.5 mm) was purchased by Amazon (Manufacturer: Santuo). Solvents were purchased from commercial sources.

2.2. Synthesis of r-BS

r-BS was synthesised by the same method as reported previously [21]. Specifically, boron and sulfur were mixed in a 1:1 atomic ratio in a mortar, and the mixture was pressed at 200 kgf cm^{-2} to form pellets. The pellets were packed in hexagonal boron nitride capsules, sandwiched between NaCl discs, and then sandwiched between graphite discs to prepare cells. The cells were heated at 1873 K for 40 min under a uniaxial pressure of 5.5 GPa using a belt-type high-pressure apparatus with a cylinder bore diameter of approximately 32 mm [22]. The cells were then quenched, after which the material was removed from the cells and crushed with a mortar and pestle into a powder.

2.3. Preparation of r-BS + G ink

r-BS powder (5 mg) and GNP (10 mg) were suspended in ethanol (1 mL) and sonicated for 1 h as the preparation of r-BS + G. Then, 50 μL of a Nafion solution was added to the r-BS + G mixture in ethanol to prepare the ink of r-BS + G. Samples with varying r-BS to GNP mass ratios were prepared while maintaining the same amount of r-BS (5 mg).

2.4. Preparation of B + S + G ink

To prepare the ink of B + S + G mixture, boron (1.25 mg), sulfur (3.75 mg), and GNP (10 mg) were dispersed in ethanol (1 mL) along with 50 μL of Nafion, and the dispersion was sonicated for 1 h. The boron/sulfur atomic ratio was 1:1, i.e., the same ratio as that used to synthesise r-BS. Similarly, the B + S mixture to GNP mass ratio was 1:2, i.e., the same ratio as that used to prepare r-BS + G.

2.5. Preparation of r-BS + CB ink and r-BS + CNT ink

r-BS powder (5 mg) and carbon black (CB) or CNTs (10 mg) were suspended in ethanol (1 mL) and sonicated for 1 h. To generate an ink for electrochemical measurements, 50 μL of a Nafion solution was added to the mixture in ethanol.

2.6. Preparation of ball-milled samples

A planetary ball-mill (Fritsch PL-7, Flitch Japan) was used to perform ball-milling, and the container (capacity 20 cm^3) and balls (diameter 1 cm) were made of ZrO_2. r-BS (100 mg) and six balls were put into the container, and milling was performed at atmospheric pressure, a temperature of ~300 K, and a rotation speed of 400 rpm. Each cycle involved 5 min of rotation followed by a rest time of 30 s (the rest time was introduced to prevent a temperature rise during long-time operation). Ball-milling was performed for 15 min, 30 min, or 45 min. The ball-milled sample was named with the ball-milling time, for example, the r-BS sample that was ball-milled for 30 min was named "ball-milled 30 min r-BS". The sample inks of ball-milled r-BS + G were prepared as the same way with the r-BS + G sample ink.

2.7. Preparation of other comparison sample inks

For other comparison sample inks, 5 mg of sample (RuO_2, GNP, or r-BS) was suspended in ethanol (1 mL) with 50 μL of a Nafion solution, and sonicated for 30 min before measurement.

2.8. Preparation of r-BS-NF electrode and RuO_2-NF electrode

r-BS or RuO_2 (5 mg) was dispersed in ethanol (1 mL) containing Nafion (50 μL), and the dispersion was sonicated for 20 min to obtain an ink for subsequent electrochemical measurements. Then, the ink (50 μL) was dropped on a pre-treated and cleaned piece of Ni foam (NF; 0.5 cm × 1.5 cm × 1.5 mm) to afford the working electrode. The pre-treatment of Ni foam for the cleaning is as follows: sonicate in acetone to remove surface oil stains, soak in 20% hydrochloric acid (5 min) to remove surface oxide film, and ultrasonic cleaning using distilled water and ethanol in sequence.

2.9. Characterisation

Powder X-ray diffraction (XRD) analysis was performed using a Rigaku MiniFlex (Tokyo, Japan) instrument with a Cu Kα X-ray source (wavelength $\lambda = 1.540598$ Å). Diffraction patterns were recorded using a D/teX Ultra silicon strip detector (Rigaku) at a speed of 0.05° s^{-1} up to $2\theta = 80°$, where θ is the angle of incidence. Scanning electron microscopy (SEM) and electron-probe microanalysis were performed using a JXA-8530F instrument (JEOL, Ltd., Japan) at an operating voltage of 10 kV. Raman spectroscopy was conducted using a multichannel Raman imaging system (ST Japan Inc., Japan) at an incident wavelength of 532 nm. Transmission electron microscopy (TEM) and scanning TEM (STEM) images were captured using a JEM-2100F TEM/STEM microscope (JEOL, Ltd., Japan) equipped with an energy-dispersive X-ray spectrometer operating at 200 kV. Double spherical aberration (Cs)

correctors (CEOS GmbH, Heidelberg, Germany) were used to obtain high-contrast images with a point-to-point resolution of 1.4 Å. Energy-dispersive X-ray spectroscopy (EDS) profiles were collected using a JEOL JED-2300 T instrument. X-ray photoelectron spectroscopy (XPS) measurements were conducted using a JPS 9010 TR spectrometer (JEOL Ltd., Japan) equipped with a Mg Kα X-ray source ($\lambda = 1253.6$ eV). The sample was placed on a piece of graphite tape. As charge accumulation in the sample shifted the binding energy to higher values, the charge-up amount was calibrated using the C 1s peak of graphene and graphite tape at 284.6 eV. Particle size distributions of the electrolyte at different conditions were measured by dynamic light scattering using nano SAQLA (Otsuka Denshi, Osaka, Japan). Specific surface area of the samples was examined by the Brunauer-Emmett-Teller (BET) method using nitrogen adsorption and desorption isotherms by BELSORP-MAX G machine and its software (Microtrack Bell, Japan).

2.10. Electrochemical measurements

All electrochemical measurements were performed on a Corrtest CS2350H electrochemical workstation in 1 M aqueous KOH. The standard three-electrode setup consisted of an active material–loaded glassy carbon electrode (GCE) as the working electrode, a platinum wire counter electrode, and Hg/HgO (1 M KOH, aqueous) as the reference electrode. Except for the active material, all electrodes were purchased from BAS Inc., Japan. For each measurement, the prepared ink (15 μL) was dropped thrice onto the polished surface of the GCE to achieve a final catalyst loading of 0.225 mg cm^{-2}. Linear sweep voltammetry (LSV) curves were recorded at a scan rate of 2 mV s^{-1}, and the obtained potential was subjected to iR correction. The LSV curves recorded before and after 500 cyclic voltammetry (CV) cycles (1.20–1.53 V vs. reversible hydrogen electrode (RHE), scan rate = 100 mV s^{-1}) were compared to evaluate the electrocatalytic stability of the catalysts. The double-layer capacitance (C_{dl}) was used to examine the electrochemically active surface area in the potential range of 0.82–0.92 V vs. RHE. Electrochemical impedance spectroscopy measurements were performed in the frequency range of 10^5–10^{-1} Hz at 1.7 V vs. RHE with an amplitude of 5 mV.

All experiments were carried out at ambient temperature (298 ± 2 K), and the standard electrode potential of Hg/HgO/1.0 M KOH (MMO, mercury/mercury oxide) was 0.108 V vs standard hydrogen electrode (SHE) based on the manufacturer's specification. Then, the potential of the Hg/HgO/1.0 M KOH reference electrode was calculated to the RHE scale at pH 14 as follows [23]:

$$E(\mathrm{RHE}) = E(\mathrm{Hg/HgO}) + 0.0591 \times \mathrm{pH} + 0.108 = E(\mathrm{Hg/HgO}) + 0.935\ \mathrm{V}.$$

Thus, the reversible potential of water oxidation, 1.23 V vs. RHE at pH 14, was calculated as 0.295 V vs. Hg/HgO/1.0 M KOH at pH 14 (1.230 V − 0.935 V = 0.295 V).

2.11. iR correction

Ohmic loss correction was carried out for polarisation curves recorded on different support surfaces as

$$E_{\mathrm{corrected}} = E - iR_{\mathrm{u}},$$

where $E_{\mathrm{corrected}}$ is the iR-corrected potential, E is the measured potential, i is the measured current, and R_{u} is the solution series resistance measured by electrochemical impedance spectroscopy.

2.12. Faradaic efficiency calculation

The Faradaic efficiency (FE) was calculated as

$$\mathrm{FE} = \frac{I_{\mathrm{ring}}}{C_{\mathrm{e}} \times I_{\mathrm{disc}}},$$

where I_{disc} is the given current on the disc electrode and I_{ring} is the current collected on the platinum electrode at a constant potential of 0.40 V vs. RHE. This potential was selected to reduce the oxygen gas evolution on the disc electrode at a rotation rate of 1600 rpm in argon-saturated 1 M KOH. C_{e} is the oxygen collection coefficient (0.2) for this type of electrode configuration [17,24].

3. Results and discussion

3.1. Characterisation of r-BS + G

r-BS was synthesised by a previously reported high-pressure solid-state reaction [21], wherein a mixture of amorphous boron and sulfur with an atomic ratio of 1:1 was formed into a pellet and heated to 1873 K at 5.5 GPa. r-BS is a layered material with trigonal symmetry structure and an $R\ \bar{3}\ m$ space group (Fig. 1a). XRD analysis corroborated the single-phase nature of the synthesised r-BS powder (Fig. S1a) [21]. SEM analysis (Fig. S1b) revealed that most of the r-BS powder particles were larger than 10 μm, while some were only a few hundred nanometres in size. Raman spectroscopy (Fig. S1c) and XPS (Fig. S1d and S1e) of the as-synthesised r-BS powder provided results consistent with those reported previously [21], without demonstrating the presence of any other crystal phase, and thus indicated that the obtained r-BS powder was single phase. Because r-BS powder prepared by the method used here is a p-type semiconductor [25,26], its electrical conductivity must be increased to use it as an OER electrocatalyst. Therefore, we incorporated GNP into the r-BS. To prepare the r-BS + G mixture, r-BS powder and GNP were combined in ethanol and then exposed to bath sonication. TEM analysis of the r-BS + G powder showed that the r-BS was well supported by the graphene (Fig. 1b). The smaller dark objects in the TEM images correspond to r-BS, as verified by elemental mapping using EDS (Fig. 1c). The full-range EDS (Fig. S2a) and XPS (Fig. S2b) analyses of the r-BS + G samples detected only four elements (B, S, C, and O); thus, there are no impurity elements that might otherwise contribute to the OER. This conclusion was supported by the results of electrochemical measurements performed using only graphene or only r-BS, as discussed in Section 3.2.

The SEM images and corresponding elemental mapping results of r-BS + G further indicate that r-BS and GNP maintained their morphologies in the mixture after the addition of Nafion (Fig. S3). This mixture incorporating Nafion was subsequently used for electrocatalytic performance measurements.

3.2. Electrocatalytic performance of r-BS + G

The electrocatalytic performance of the r-BS + G powder was investigated using a three-electrode system in an alkaline electrolyte (1 M KOH) and compared to that of commercially available RuO_2 as a reference. LSV was performed to obtain polarisation curves, which were corrected using iR-compensation. As depicted in Fig. 2a and b, r-BS + G exhibited high OER activity with an overpotential of 250 mV at 10 mA cm^{-2}. This overpotential is 50 mV lower than that of commercial RuO_2 and lower than that of most reported OER electrocatalysts [17,19,24,27,28] (Table S1). Importantly, both r-BS and GNP exhibited inferior OER performance when evaluated independently. This result indicates that no impurity elements contributed to the OER performance in either the GNP or synthesised r-BS samples, which is consistent with the results of the EDS and XPS analyses in Section 3.1. Furthermore, CV curves were recorded at 10 mV s^{-1} using the r-BS + G catalyst, which confirmed that no iron content due to the aqueous solution affected the electrochemical performance (Fig. S4) [29]. Moreover, a simple mixture of boron, sulfur, and GNP (B + S + G, Fig. S5a) did not show good OER performance. These results show that the high OER activity purely arises from the prepared r-BS + G.

The above results confirm that the mixture of r-BS and GNP is key to

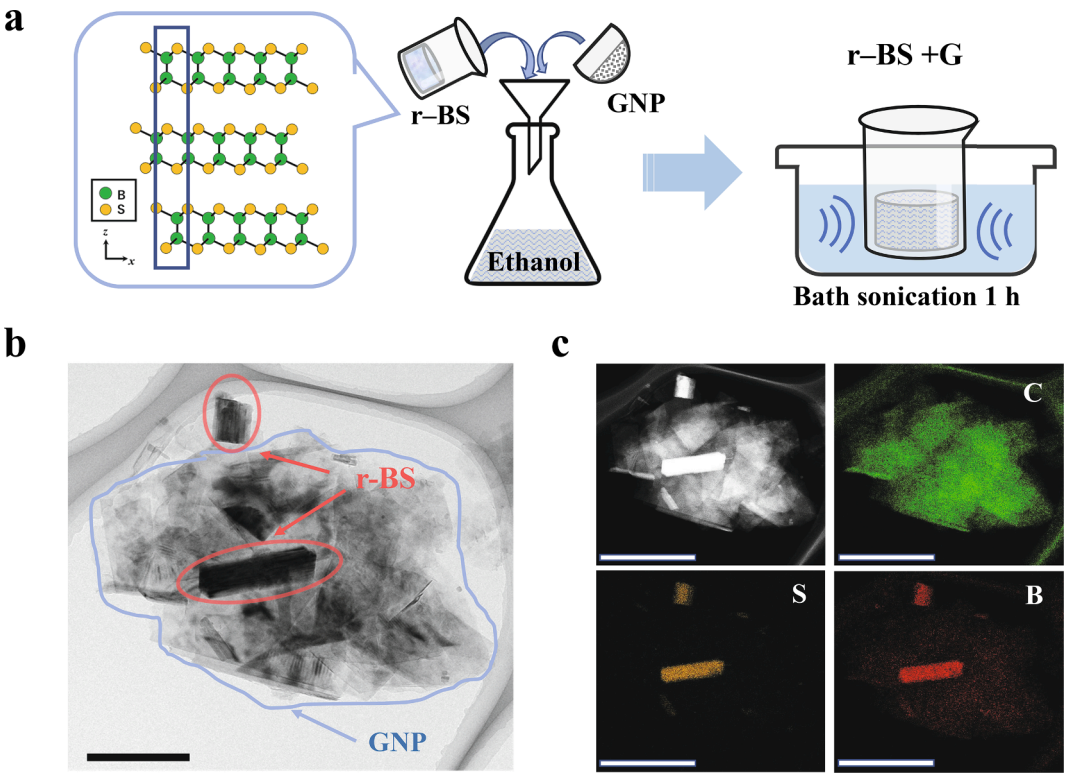

Fig. 1. Preparation of r-BS + G catalyst. (a) Schematic of the preparation method of r-BS + G. (b) TEM image of r-BS + G. Scale bar: 500 nm. (c) High-angle annular dark-field STEM image and elemental mapping images of r-BS + G by EDS in STEM. Scale bars: 1.0 μm.

the increased OER catalytic activity of the r-BS + G catalyst. The mixing ratio between r-BS and GNP was found to affect the catalytic activity (Fig. S5b), with a r-BS/GNP weight ratio of 1:2 providing the best performance (Table S2). When the r-BS/GNP weight ratio increased to 1:3, the catalytic performance decreased. In the SEM images (Fig. S6), many r-BS particles were covered by excess GNPs, which might block some active sites and lower the OER performance. Furthermore, a r-BS/GNP weight ratio of 1:1 offered lower catalytic activity owing to inadequate electrical conductivity. Indeed, SEM image (Fig. S6) shows aggregation of r-BS powders in the case of 1:1. The choice of carbon material also substantially influenced the catalytic properties. When GNP was replaced with CNTs or CB, the activity decreased significantly (Table S2), probably because the nanosheets of GNP acted as an ideal support for the r-BS powder, whereas the other carbon sources did not establish good interaction with r-BS (Fig. S5c). To verify this hypothesis, electrochemical impedance spectroscopy (EIS) measurements and SEM observations were conducted, as shown in Fig. S7. The EIS data were used to estimate R_u as 1.15, 2.54, and 2.25 Ω for r-BS + G, r-BS + CB, and r-BS + CNT, respectively. The smallest R_u value of r-BS + G indicates that GNP is the most effective at improving conductivity. SEM images of these three samples also clearly indicate the difference in their morphologies (Figs. S7b–d). GNP consisted of smaller particles and formed closer connections with the r-BS particles compared with the other two samples, implying a larger improvement in conductivity that is consistent with the EIS results (Fig. S7a). These additional data thus suggest that the best OER performance of r-BS + G is owing to better contact with the r-BS particles.

For the commercial RuO_2 catalyst, the OER started when the applied potential reached 1.47 V. However, by this voltage, the r-BS + G catalyst already had an OER current density of 7 mA cm^{-2} (Fig. 2a). The electrochemical measurements showed that the r-BS + G catalyst had a Tafel slope of 210 mV dec^{-1}, which is quite high compared to that of RuO_2 (Fig. 2c). This indicates that the rate determining process is different for the r-BS + G and RuO_2 catalysts and/or that different reactions occur on them. A self-supported working electrode (r-BS on Ni foam, r-BS-NF) was prepared by impregnating cleaned Ni foam with a GNP-free sample ink containing only r-BS. As shown in Fig. S8a, the r-BS-NF electrode outperformed RuO_2 on Ni foam (RuO_2-NF). Replacing the GNP support with NF decreased the Tafel slope from 210 to 61 mV dec^{-1} (Fig. 2c and S8b), which is comparable to that of RuO_2. This result suggests that a small Tafel slope can be realised for r-BS by selecting an appropriate support material.

The stability of the r-BS + G catalyst was also investigated using CV. As shown in Fig. 2d, after 500 CV cycles between 1.20 and 1.53 V, the performance of the r-BS + G catalyst experienced negligible degradation, demonstrating its durability. In addition, its morphology hardly changed after 500 CV cycles (Fig. S9), whereas the commercial RuO_2 catalyst did not maintain its activity after 500 CV cycles between 1.20 and 1.53 V (Fig. S10a). However, after 2000 CV cycles, the performance of the r-BS + G catalyst degraded notably (Fig. S10b), presumably because the r-BS particles detached from the electrode surface and/or underwent undesirable reactions to form other phases during cycling (Fig. S10c-d).

To determine whether the electrochemical current in Fig. 2a originates from the OER or another reaction, the Faradaic efficiency was measured. A rotating ring–disc electrode (RRDE) was used, whereby the OER was realised on the disc electrode and the ORR proceeded on the ring electrode. The disc current was set at a constant value of 300 μA to generate oxygen bubbles *in situ*. The formed oxygen was simultaneously reduced by sweeping across the platinum ring electrode with an ORR potential of 0.40 V (vs. RHE). As shown in Fig. 2e, when the applied disc current was set at 300 μA, the detected ring current was approximately 59.3 μA, corresponding to a Faradaic efficiency of 98.8% (the collection efficiency was set at 0.2) [30,31]. This result indicates that the electrochemical current mainly comes from the OER.

To further examine the gas evolution across the entire potential sweep range, the potential of the disc electrode was scanned over the range identical to that used for the OER in Fig. 2a, where the platinum

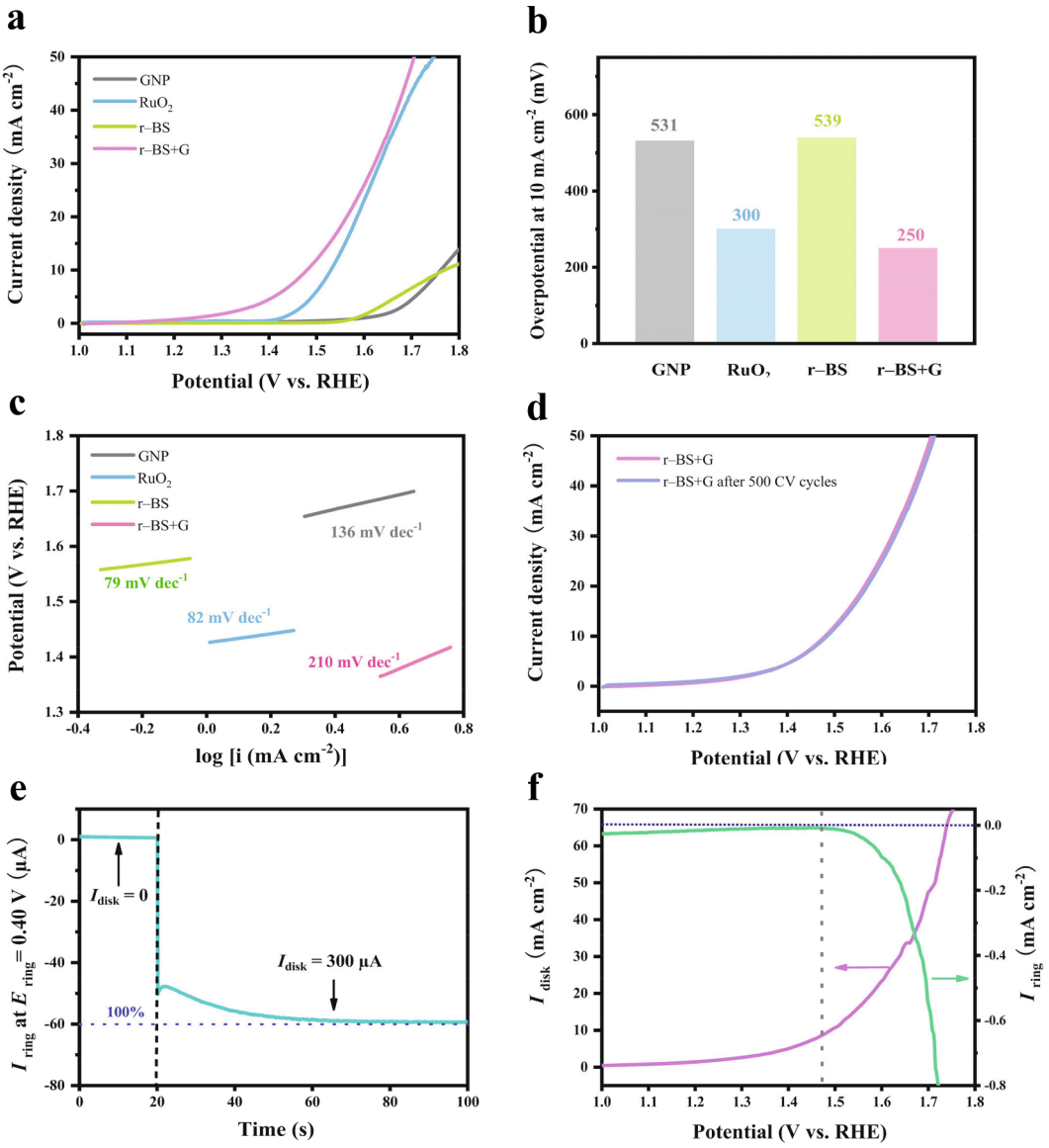

Fig. 2. OER performances of various electrocatalysts. (a) LSV curves for the OER, (b) overpotentials at 10 mA cm^{-2}, and (c) Tafel plots of various electrocatalysts. (d) LSV curves of r-BS + G recorded before and after 500 CV cycles between 1.20 and 1.53 V, (e) Faraday efficiency testing of r-BS + G using the rotating ring–disc electrode (RRDE) technique in Ar-saturated 1 M KOH solution. The vertical dashed black line points to the time at which a 300-μA current was applied to the disc electrode, while the horizontal dashed blue line corresponds to the calculated 100% efficiency (60 μA). (f) Disc current at the r-BS + G/glassy carbon disc electrode in Ar-saturated 1 M KOH (pink) and Pt ring (held at 0.2 V vs. RHE) current due to the ORR (green) as functions of the disc potential. The vertical dashed grey line shows the onset of the ORR at the ring electrode. (For interpretation of the references to colour in this figure legend, the reader is referred to the web version of this article.)

ring electrode was held at a constant potential of 0.2 V (vs. RHE) and both the ring current and disk current were recorded [32]. Before starting the measurement, the electrolyte was purged with argon gas for 30 min to remove any dissolved oxygen. In addition, the reaction system was blanketed with an argon atmosphere above the liquid surface during the measurement. Fig. 2f shows the disc and ring currents measured in 1 M KOH at 1600 rpm with a scan rate of 10 mV s^{-1}. When the potential of the disc electrode was swept over 1.48 V (250 mV of overpotential), a marked increase in ring current was observed. As this ring current was caused by the ORR due to the potential limitation, the bubbles that formed at the disc electrode were attributed to oxygen gas.

Furthermore, the absolute value of the ring current increased as the sweeping potential increased. This result indicates that the oxygen gas evolved at the disc electrode was concomitantly reduced at the ring electrode over the disc potential range. Thus, we clarified that the electrochemical current of r-BS + G in the whole swept potential range in Fig. 2a mainly originated from the OER.

To gain more insight into the catalytic activity of the r-BS + G catalyst, the kinetics of the electrode reactions were investigated using EIS (Fig. S5d and Table S3). r-BS had a large R_u of 6.58 Ω, whereas incorporating GNP into r-BS considerably decreased R_u to 1.15 Ω, which indicates that the conductivity was greatly increased by the presence of GNP. On the other hand, the r-BS + G electrode had a charge transfer resistance of 8.40 Ω, which was smaller than that of RuO_2 (10.87 Ω) and significantly smaller than those of r-BS (18.56 Ω) and graphene (43.51 Ω). These results indicate that the electrocatalytic performance of r-BS was realised by mixing with graphene. Next, the electrochemically active surface areas of the as-prepared r-BS + G and r-BS catalysts were evaluated via C_{dl} measurements (Fig. S11), because C_{dl} is proportional to the charge-induced surface area. The C_{dl} of r-BS + G was considerably higher than that of r-BS, indicating a significantly larger electroactive surface area.

3.3. Stability of r-BS + G against OER

Fig. 3a shows XRD patterns of the r-BS + G catalyst before and after 500 CV cycles. Both patterns were nearly identical to the combined patterns of r-BS and GNP, confirming the absence of additional phase formation during cycling. In addition, the crystal structure of the material remained stable during CV cycling in KOH solution. The full-range XPS scan of r-BS + G revealed O 1s, F 1s, C 1s, B 1s, and S 2p peaks (Fig. 3b). Except for the potassium signal caused by K^+ adsorption from the KOH solution, no impurities were found in the sample after the CV measurement (Fig. S12b). The B 1s and S 2p spectra of r-BS + G under various conditions are presented in Fig. 3c and d, respectively. The peak positions of B 1 s (189.0 eV) and S 2p (162.8 eV) of r-BS + G were consistent with those previously reported for r-BS [21]. After the LSV measurement, slight shifts were observed for both the B 1s and S 2p peaks, and a new peak appeared at ~168 eV, which corresponds to a small amount of sulfate species [33] due to the strongly oxidising potentials. The B 1s and S 2p peaks were also widened after electrochemical measurements, probably due to the adsorbed species that slightly modified the electronic states of r-BS. However, no peaks of oxidised boron were detected. The slight shifting of the B 1s and S 2p peaks was probably also due to the effect of adsorbates left on the r-BS surface. As shown in Fig. 3c and d, after 500 CV cycles, the XPS profile did not change, which indicates that the chemical states of the r-BS + G surface did not change during cycling.

The Raman spectra of r-BS + G recorded under various conditions are shown in Fig. 3e and f. There are three distinct peaks in the lower wavenumber region at 319, 687, and 1041 cm^{-1}, which can be attributed to the $A_1(3)$, E(4), and $A_1(4)$ modes of r-BS, respectively (Fig. S1c) [34]. Wide-range Raman spectra (Fig. 3f) further ruled out any major spectral changes (such as peak shifts or (dis)appearance) in r-BS + G during electrochemical measurements. In addition, the major peaks in the wide-range Raman spectrum were almost the same as those observed for the graphene-only case in Fig. S12c. These results clearly demonstrate the stability of the as-prepared r-BS + G catalyst, providing a basis for its future applications.

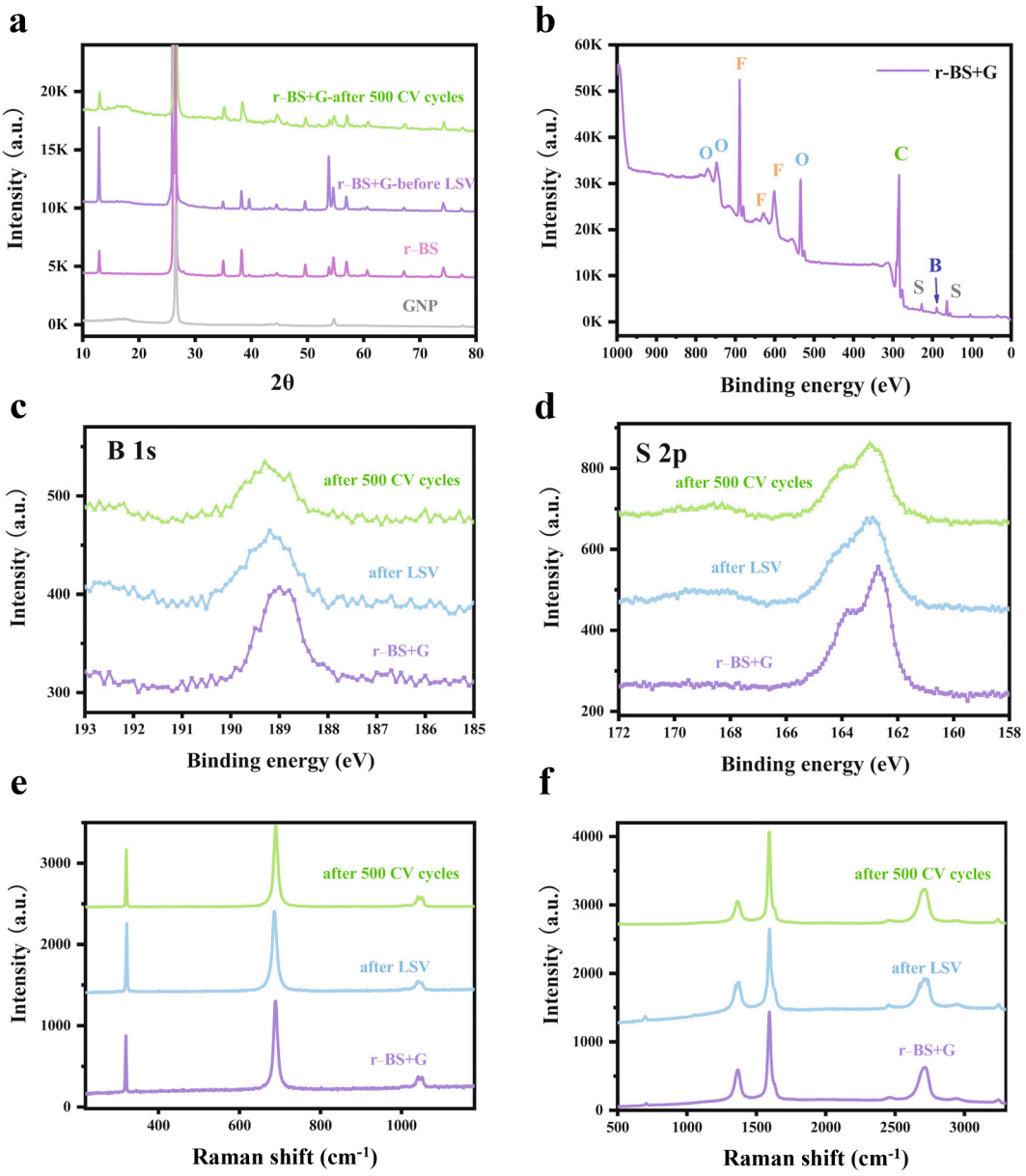

Fig. 3. Electronic structural characterisation of r-BS + G. (a) XRD patterns of various electrocatalysts. (b) Full-range X-ray photoelectron spectrum of r-BS + G. High-resolution (c) B 1s and (d) S 2p spectra of r-BS + G recorded under different conditions. (e) Narrow- and (f) wide-range Raman spectra of r-BS + G.

3.4. Active sites

Now, we would discuss the active sites of r-BS based on the experimental data and preliminary theoretical calculation. First, we evaluated the catalytic active sites of r-BS based on the electrocatalytic performance of ball-milled r-BS samples. Next, we performed the DFT calculation with the thermodynamic computational hydrogen electrode (CHE) model stablished by Nørskov et al. [36] for the pristine r-BS and model-defected r-BS surfaces (Further computational details can be found in the Supplementary Information). Finally, we discuss the possible active sites and future works to enhance the OER activity of r-BS electrocatalyst.

First, we experimentally evaluated the catalytic active sites of r-BS based on the electrocatalytic performance of ball-milled r-BS samples. In addition to the similarity in crystal structure, the electronic structure of r-BS is also similar to that of MoS_2. That is, the bandgap of r-BS can be adjusted by controlling the number of layers. It increases from 2.7 eV for multilayer r-BS to 3.6 eV for monolayer r-BS [21]. The active sites of MoS_2 for the HER have been discussed in detail, and the mainstream opinion is that, because the active sites of MoS_2 are related to the edges, the catalytic activity increases as the area of exposed edges increases [35]. Hence, as a first approach, we investigated the active sites of r-BS following the strategy for MoS_2, although the reaction here is the OER instead of the HER. In line with this strategy, we attempted to increase the area of exposed edges in r-BS by decreasing its particle size via ball-milling. As illustrated in Figs. S13a, ball-milling did not affect the XRD pattern of r-BS, except for inducing peak broadening. The crystal sizes calculated based on the Scherrer equation are shown in Table S4. The surface area was measured by Brunauer–Emmett–Teller (BET) analysis as shown in Fig. S13b. After ball-milling for 45 min, the crystallite size decreased from 34 to 26 nm, whereas the surface area increased from 1.35 to 9.85 m^2/g. These results suggest a concomitant increase in the area of exposed edges. Indeed, SEM analysis of the ball-milled r-BS (Fig. S13c) demonstrated that it had a reduced particle size and increased area of edge sites compared to the original r-BS (Fig. S1b). XPS profiles of the ball-milled r-BS are shown in Figs. S13d and S13e. After ball-milling for 30 min, additional peak components appeared in both the B 1s and S 2p regions at higher energies than the original peak energies, indicating that part of the surface and/or the exposed edges sites were slightly oxidised. The ball-milled r-BS samples were mixed with the same proportion of graphene before activity testing (Fig. S13f); however, the performance was found to deteriorate with increasing ball-milling time.

Next, as a preliminary theoretical consideration, we discuss the DFT result of the free-energy barriers of OER intermediates at the r-BS (0001) surface. As shown in Figs. S15a and S15b, a high free-energy barrier exists under a bias voltage at the pristine r-BS surface to produce *OOH intermediates from *O, which indicates that pristine r-BS alone is not a good OER catalyst. To consider the effect of the graphene sheets, we also performed DFT calculations for the r-BS + G system and found no qualitative differences in the adsorption free energies. Then, we performed DFT calculations using a model defective r-BS surface. As the model defected surfaces, the boron vacant (V_B) and carbon-atom-doped r-BS surfaces were employed, whereby active sites were assumed as the S atom around V_B and the doped C atom to the outermost S site. After introducing V_B, the maximum energy barrier is drastically decreased from that for the pristine r-BS, and carbon-atom doping further reduces the limiting potential (Figs. S15a and S15b). Moreover, V_B and carbon-atom doping created unoccupied states in the bandgap, as shown in the projected density of states for r-BS with and without the defects (Fig. S15f). The Kohn–Sham level density for the defected surfaces were distributed around the defect sites at the outermost surface (right panels in Fig. S15f), which differs from the densities at the pristine surface. This suggests that the surface-localised states can alter the adsorption energy of the OER intermediates and that defect sites can function as active sites in r-BS. As discussed above, we computationally demonstrated the relationship between the defect-induced electronic structure and the adsorption energies of the OER intermediates.

Finally, we discuss the possible active sites of r-BS electrocatalyst based on our experimental and DFT data and considerable future work to enhance the OER activity using r-BS electrocatalyst. Our experimental data of ball-milled r-BS show that the catalytic performance of r-BS + G was not improved by increasing the surface area and area of exposed edges of r-BS. Thus, the graphene mainly plays a role of the conductive assistant, and the active sites tend to correspond to specific surface sites of r-BS rather than to all surface atoms or only edge atoms. According to the recent conductivity measurements, synthesised r-BS shows the p-type conductivity [25,26], which might come from the high pressure and high temperature preparation. Therefore, intrinsic defects at the surface are considered to play a role in the active site. The theoretical results for the pristine r-BS with and without the graphene sheet support the discussion based on the experimental data. Thus, to enhance the OER activity of the r-BS electrode, further active sites may need to be introduced at the r-BS surface. The results of the defected r-BS surface gains the following two important insights into the active site of r-BS: (1) The defect induced state can tune the thermodynamic stability of the OER intermediates, (2) By controlling the defect state, we can enhance the OER activity of r-BS-based electrocatalyst. The former suggests that the electronic structure induced by the surface defect in the experiment might be close to the model defected surfaces used in the DFT calculation. The latter motivates us to control the surface electronic state by engineering the surface defect, which is important for enhancing the OER activity of r-BS. Therefore, as a next step, we need to specify the active site by both experimental and theoretical studies as followings: In experiment, to determine the active sites in r-BS + G, future studies will involve atomic-scale microscopy and further spectroscopy studies on well-defined and defect-controlled model catalysts. Theoretically, further comprehensive studies on the relationship between the OER activity and possible intrinsic defects at the r-BS/aqueous solution interface are necessary to fully understand the catalytic mechanism of r-BS + G [37]. Although the active sites in r-BS + G were not specified in this study, we demonstrate that synthesised r-BS + G shows the high OER performance as discussed above. Therefore, we believe that the r-BS + G is a new class of the OER catalyst composed of abundant elements.

4. Conclusions

A new OER electrocatalyst exhibiting a performance higher than that of commercial RuO_2 was developed via the hybridisation of r-BS with GNP. XRD, XPS, and Raman spectroscopy analyses confirmed that the r-BS + G catalyst had a stable structure, and a series of experiments were carried out to examine its active sites. Ball-milling experiments and DFT calculations using the CHE model indicated that the catalytically active sites are possibly defect sites. Controlling the number of r-BS active sites may further enhance the OER performance of r-BS + G. Thus, r-BS shows promise as a parent material for the fabrication of efficient, low-cost, and robust catalysts for renewable energy applications.

Declaration of Competing Interest

The authors declare that they have no known competing financial interests or personal relationships that could have appeared to influence the work reported in this paper.

Data availability

Data will be made available on request.

Acknowledgements

This work was supported by the Japan Science and Technology

Agency (JST) through the Adaptable and Seamless Technology Transfer Program through Target-driven R&D (A-STEP) [grant number JPMJTR22T4]; the MEXT Element Strategy Initiative to Form Core Research Center [grant number JPMXP0112101001]; JSPS KAKENHI [grant numbers JP18K18989, JP19H02551, JP19H05046:A01, JP20H05673, JP21H05012, JP22K18964, JP22K14643, and JP21H00015:B01 Hydrogenomics]; MHI Innovation Accelerator LLC; TIAKakehashi collaborative research program (2022); and the MEXT Program for Promoting Research on the Supercomputer Fugaku (Fugaku Battery & Fuel Cell Project) [grant number JPMXP1020200301]. Parallel computations were performed using the Fugaku supercomputer provided by the RIKEN Center for Computational Science [Project ID: hp150275 and hp220088] and FLOW provided by Nagoya University. The sponsors had no involvement in the study design; in the collection, analysis, or interpretation of data; in the writing of the report; or in the decision to submit the article for publication.

Appendix A. Supplementary data

Supplementary data to this article can be found online at https://doi.org/10.1016/j.cej.2023.144489.

References

[1] S. Pan, H. Li, D. Liu, R. Huang, X. Pan, D. Ren, J. Li, M. Shakouri, Q. Zhang, M. Wang, C. Wei, L. Mai, B. Zhang, Y. Zhao, Z. Wang, M. Graetzel, X. Zhang, Efficient and stable noble-metal-free catalyst for acidic water oxidation, Nat. Commun. 13 (2022) 2294, https://doi.org/10.1038/s41467-022-30064-6.

[2] F. Cheng, J. Shen, B. Peng, Y. Pan, Z. Tao, J. Chen, Rapid room-temperature synthesis of nanocrystalline spinels as oxygen reduction and evolution electrocatalysts, Nat. Chem. 3 (2011) 79–84, https://doi.org/10.1038/nchem.931.

[3] C. Yang, G. Rousse, K.L. Svane, P.E. Pearce, A.M. Abakumov, M. Deschamps, G. Cibin, A.V. Chadwick, D.A.D. Corte, H.A. Hansen, T. Vegge, J.-M. Tarascon, A. Grimaud, Cation insertion to break the activity/stability relationship for highly active oxygen evolution reaction catalyst, Nat. Commun. 11 (2020) 1378, https://doi.org/10.1038/s41467-020-15231-x.

[4] N.T. Suen, S.-F. Hung, Q. Quan, N. Zhang, Y.-J. Xu, H.M. Chen, Electrocatalysis for the oxygen evolution reaction: recent development and future perspectives, Chem. Soc. Rev. 46 (2017) 337–365, https://doi.org/10.1039/C6CS00328A.

[5] H.N. Nong, L.J. Falling, A. Bergmann, M. Klingenhof, H.P. Tran, C. Spöri, R. Mom, J. Timoshenko, G. Zichittella, A. Knop-Gericke, S. Piccinin, J. Pérez-Ramírez, B. R. Cuenya, R. Schlögl, P. Strasser, D. Teschner, T.E. Jones, Key role of chemistry versus bias in electrocatalytic oxygen evolution, Nature 587 (2020) 408–413, https://doi.org/10.1038/s41586-020-2908-2.

[6] Z.-F. Huang, S. Xi, J. Song, S. Dou, X. Li, Y. Du, C. Diao, Z.J. Xu, X. Wang, Tuning of lattice oxygen reactivity and scaling relation to construct better oxygen evolution electrocatalyst, Nat. Commun. 12 (2021) 3992, https://doi.org/10.1038/s41467-021-24182-w.

[7] L. Cao, Q. Luo, J. Chen, L. Wang, Y. Lin, H. Wang, X. Liu, X. Shen, W. Zhang, W. Liu, Z. Qi, Z. Jiang, J. Yang, T. Yao, Dynamic oxygen adsorption on single-atomic ruthenium catalyst with high performance for acidic oxygen evolution reaction, Nat. Commun. 10 (2019) 4849, https://doi.org/10.1038/s41467-019-12886-z.

[8] N. Li, R.G. Hadt, D. Hayes, L.X. Chen, D.G. Nocera, Detection of high-valent iron species in alloyed oxidic cobaltates for catalysing the oxygen evolution reaction, Nat. Commun. 12 (2021) 4218, https://doi.org/10.1038/s41467-021-24453-6.

[9] S. Yuan, J. Peng, B. Cai, Z. Huang, A.T. Garcia-Esparza, D. Sokaras, Y. Zhang, L. Giordano, K. Akkiraju, Y.G. Zhu, R. Hübner, X. Zou, Y. Román-Leshkov, Y. Shao-Horn, Tunable metal hydroxide-organic frameworks for catalysing oxygen evolution, Nat. Mater. 21 (2022) 673–680, https://doi.org/10.1038/s41563-022-01199-0.

[10] S. Liu, S. Geng, L. Li, Y. Zhang, G. Ren, B. Huang, Z. Hu, J.-F. Lee, Y.-H. Lai, Y.-H. Chu, Y. Xu, Q. Shao, X. Huang, A top-down strategy for amorphization of hydroxyl compounds for electrocatalytic oxygen evolution, Nat. Commun. 13 (2022) 1187, https://doi.org/10.1038/s41467-022-28888-3.

[11] F. Lyu, Q. Wang, S.M. Choi, Y. Yin, Noble-metal-free electrocatalysts for oxygen evolution, Small 15 (1) (2019), e1804201, https://doi.org/10.1002/smll.201804201.

[12] W. Xiang, N. Yang, X. Li, J. Linnemann, U. Hagemann, O. Ruediger, M. Heidelmann, T. Falk, M. Aramini, S. DeBeer, M. Muhler, K. Tschulik, T. Li, 3D atomic-scale imaging of mixed Co-Fe spinel oxide nanoparticles during oxygen evolution reaction, Nat. Commun. 13 (2022) 179, https://doi.org/10.1038/s41467-021-27788-2.

[13] A. Li, S. Kong, C. Guo, H. Ooka, K. Adachi, D. Hashizume, Q. Jiang, H. Han, J. Xiao, R. Nakamura, Enhancing the stability of cobalt spinel oxide towards sustainable oxygen evolution in acid, Nat. Catal. 5 (2022) 109–118, https://doi.org/10.1038/s41929-021-00732-9.

[14] Z. He, J. Zhang, Z. Gong, H. Lei, D. Zhou, N. Zhang, W. Mai, S. Zhao, Y. Chen, Activating lattice oxygen in NiFe-based (oxy)hydroxide for water electrolysis, Nat. Commun. 13 (2022) 2191, https://doi.org/10.1038/s41467-022-29875-4.

[15] H.B. Yang, J. Miao, S.-F. Hung, J. Chen, H.B. Tao, X. Wang, L. Zhang, R. Chen, J. Gao, H.M. Chen, L. Dai, B. Liu, Identification of catalytic sites for oxygen reduction and oxygen evolution in N-doped graphene materials: Development of highly efficient metal-free bifunctional electrocatalyst, Sci. Adv. 2 (2016), e1501122, https://doi.org/10.1126/sciadv.1501122.

[16] J. Zhang, Z. Zhao, Z. Xia, L. Dai, A metal-free bifunctional electrocatalyst for oxygen reduction and oxygen evolution reactions, Nat. Nanotechnol. 10 (2015) 444–452, https://doi.org/10.1038/nnano.2015.48.

[17] C. Mo, J. Jian, J. Li, Z. Fang, Z. Zhao, Z. Yuan, M. Yang, Y. Zhang, L. Dai, D. Yu, Boosting water oxidation on metal-free carbon nanotubes via directional interfacial charge-transfer induced by an adsorbed polyelectrolyte, Energy Environ. Sci. 11 (2018) 3334–3341, https://doi.org/10.1039/C8EE01487F.

[18] Z. Liu, J. Ai, M. Sun, F. Han, Z. Li, Q. Peng, Q.-D. Wang, J. Liu, L. Liu, Phosphorous-doped graphite layers with outstanding electrocatalytic activities for the oxygen and hydrogen evolution reactions in water electrolysis, Adv. Funct. Mater. 30 (2020) 1910741, https://doi.org/10.1002/adfm.201910741.

[19] Q. Hu, G. Li, X. Liu, B. Zhu, X. Chai, Q. Zhang, J. Liu, C. He, Superhydrophilic phytic-acid-doped conductive hydrogels as metal-free and binder-free electrocatalysts for efficient water oxidation, Angew. Chem. Int. Ed. 58 (2019) 4318–4322, https://doi.org/10.1002/anie.201900109.

[20] Z. Liu, Z. Zhao, Y. Wang, S. Dou, D. Yan, D. Liu, Z. Xia, S. Wang, In situ exfoliated, edge-rich, oxygen-functionalized graphene from carbon fibers for oxygen electrocatalysis, Adv. Mater. 29 (2017), 1606207, https://doi.org/10.1002/adma.201606207.

[21] H. Kusaka, R. Ishibiki, M. Toyoda, T. Fujita, T. Tokunaga, A. Yamamoto, M. Miyakawa, K. Matsushita, K. Miyazaki, L. Li, S.L. Shinde, M.S.L. Lima, T. Sakurai, E. Nishibori, T. Masuda, K. Horiba, K. Watanabe, S. Saito, M. Miyauchi, T. Taniguchi, H. Hosono, T. Kondo, Crystalline boron monosulfide nanosheets with tunable bandgaps, J. Mater. Chem. A 9 (2021) 24631–24640, https://doi.org/10.1039/D1TA03307G.

[22] S. Yamaoka, M. Akashi, H. Kanda, T. Osawa, T. Taniguchi, H. Sei, O. Fukunaga, Development of belt type high pressure apparatus for material synthesis at 8 GPa, J. High Pressure Inst. Jpn. 30 (1992) 249–258.

[23] Y. Qi, Y. Zhang, L. Yang, Y. Zhao, Y. Zhu, H. Jiang, C. Li, Insights into the activity of nickel boride/nickel heterostructures for efficient methanol electrooxidation, Nat. Commun. 13 (2022) 4602, https://doi.org/10.1038/s41467-022-32443-5.

[24] C. Hu, L. Dai, Multifunctional carbon-based metal-free electrocatalysts for simultaneous oxygen reduction, oxygen evolution, and hydrogen evolution, Adv. Mater. 29 (2017), 1604942, https://doi.org/10.1002/adma.201604942.

[25] N. Watanabe, K. Miyazaki, M. Toyoda, K. Takeyasu, N. Tsujii, H. Kusaka, A. Yamamoto, S. Saito, M. Miyakawa, T. Taniguchi, T. Aizawa, T. Mori, M. Miyauchi, T. Kondo, Rhombohedral boron monosulfide as a p-type semiconductor, Molecules 28 (4) (2023) 1896, https://doi.org/10.3390/molecules28041896.

[26] K. Sugawara, H. Kusaka, T. Kawakami, K. Yanagizawa, A. Honma, S. Souma, K. Nakayama, M. Miyakawa, T. Taniguchi, M. Kitamura, K. Horiba, H. Kumigashira, T. Takahashi, S.-I. Orimo, M. Toyoda, S. Saito, T. Kondo, T. Sato, Direct imaging of band structure for powdered rhombohedral boron monosulfide by microfocused ARPES, Nano Lett. 23 (2023) 1673–1679, https://doi.org/10.1021/acs.nanolett.2c04048.

[27] M.-S. Balogun, W. Qiu, H. Yang, W. Fan, Y. Huang, P. Fang, G. Li, H. Ji, Y. Tong, A monolithic metal-free electrocatalyst for oxygen evolution reaction and overall water splitting, Energy Environ. Sci. 9 (2016) 3411–3416, https://doi.org/10.1039/C6EE01930G.

[28] F. Qiang, J. Feng, H. Wang, J. Yu, J. Shi, M. Huang, Z. Shi, S. Liu, P. Li, L. Dong, Oxygen engineering enables N-doped porous carbon nanofibers as oxygen reduction/evolution reaction electrocatalysts for flexible zinc–air batteries, ACS Catal. 12 (2022) 4002–4015, https://doi.org/10.1021/acscatal.2c00164.

[29] S. Anantharaj, S. Kundu, S. Noda, "The Fe Effect": A review unveiling the critical roles of Fe in enhancing OER activity of Ni and Co based catalysts, Nano Energy 80 (2021), 105514, https://doi.org/10.1016/j.nanoen.2020.105514.

[30] S. Zhao, Y. Wang, J. Dong, C.-T. He, H. Yin, P. An, K. Zhao, X. Zhang, C. Gao, L. Zhang, J. Lv, J. Wang, J. Zhang, A.M. Khattak, N.A. Khan, Z. Wei, J. Zhang, S. Liu, H. Zhao, Z. Tang, Ultrathin metal–organic framework nanosheets for electrocatalytic oxygen evolution, Nat. Energy 1 (2016) 16184, https://doi.org/10.1038/NENERGY.2016.184.

[31] U.A. Paulus, T.J. Schmidt, H.A. Gasteiger, R.J. Behm, Oxygen reduction on a high-surface area Pt/Vulcan carbon catalyst: a thin-film rotating ring-disk electrode study, J. Electroanal. Chem. 495 (2001) 134–145, https://doi.org/10.1016/S0022-0728(00)00407-1.

[32] A.T. Swesi, J. Masud, M. Nath, Nickel selenide as a high-efficiency catalyst for oxygen evolution reaction, Energy Environ. Sci. 9 (2016) 1771–1782, https://doi.org/10.1039/C5EE02463C.

[33] R.A. Marquez-Montes, K. Kawashima, Y.J. Son, J.A. Weeks, H.H. Sun, H. Celio, V. H. Ramos-Sánchez, C.B. Mullins, Mass transport-enhanced electrodeposition of Ni–S–P–O films on nickel foam for electrochemical water splitting, J. Mater. Chem. A 9 (2021) 7736–7749, https://doi.org/10.1039/D0TA12097A.

[34] K.A. Cherednichenko, P.S. Sokolov, A. Kalinko, Y. Le Godec, A. Polian, J.-P. Itié, V. L. Solozhenko, Optical phonon modes in rhombohedral boron monosulfide under high pressure, J. Appl. Phys. 117 (18) (2015), 185904, https://doi.org/10.1063/1.4921099.

[35] T.F. Jaramillo, K.P. Jørgensen, J. Bonde, J.H. Nielsen, S. Horch, I. Chorkendorff, Identification of active edge sites for electrochemical H_2 evolution from MoS_2

nanocatalysts, Science 317 (2007) 100–102, https://doi.org/10.1126/science.1141483.
[36] J.K. Nørskov, J. Rossmeisl, A. Logadottir, L. Lindqvist, J.R. Kitchin, T. Bligaard, H. Jónsson, Origin of the overpotential for oxygen reduction at a fuel-cell cathode, J. Phys. Chem. B 108 (2004) 17886–17892, https://doi.org/10.1021/jp047349j.
[37] S. Hagiwara, S. Nishihara, F. Kuroda, M. Otani, Development of a dielectrically consistent reference interaction site model combined with the density functional theory for electrochemical interface simulations, Phys. Rev. Mater. 6 (2022), 093802, https://doi.org/10.1103/PhysRevMaterials.6.093802.